Automatic Detection and Classification of Coronal Holes and Filaments Based on EUV and Magnetogram Observations of the Solar Disk

Isabelle F. Scholl · Shadia Rifai Habbal

Abstract A new method for the automated detection of coronal holes and filaments on the solar disk is presented. The starting point is coronal images taken by the Extreme Ultraviolet Telescope on the *Solar and Heliospheric Observatory* (SOHO/EIT) in the Fe IX/X 171 Å, Fe XII 195 Å, and He II 304 Å extreme ultraviolet (EUV) lines and the corresponding full-disk magnetograms from the Michelson Doppler Imager (SOHO/MDI) from different phases of the solar cycle. The images are processed to enhance their contrast and to enable the automatic detection of the two candidate features, which are visually indistinguishable in these images. Comparisons are made with existing databases, such as the He I 10830 Å NSO/Kitt Peak coronal-hole maps and the Solar Feature Catalog (SFC) from the European Grid of Solar Observations (EGSO), to discriminate between the two features. By mapping the features onto the corresponding magnetograms, distinct magnetic signatures are then derived. Coronal holes are found to have a skewed distribution of magnetic-field intensities, with values often reaching $100 - 200$ gauss, and a relative magnetic-flux imbalance. Filaments, in contrast, have a symmetric distribution of field intensity values around zero, have smaller magnetic-field intensity than coronal holes, and lie along a magnetic-field reversal line. The identification of candidate features from the processed images and the determination of their distinct magnetic signatures are then combined to achieve the automated detection of coronal holes and filaments from EUV images of the solar disk. Application of this technique to all three wavelengths does not yield identical results. Furthermore, the best agreement among all three wavelengths and NSO/Kitt Peak coronal-hole maps occurs during the declining phase of solar activity. The He II data mostly fail to yield the location of filaments at solar

I.F. Scholl (✉)
International Space University, 1 rue J.D. Cassini, 67400 Illkirch-Graffenstaden, France
e-mail: isa.scholl@gmail.com

I.F. Scholl
Laboratoire d'Études Spatiales et d'Instrumentation en Astrophysique (LESIA),
Observatoire de Paris-Meudon, Meudon, France

S.R. Habbal
University of Hawaii, 2680 Woodlawn Drive, Honolulu, HI 96822, USA
e-mail: shadia@ifa.hawaii.edu

minimum and provide only a subset at the declining phase or peak of the solar cycle. However, the Fe IX/X 171 Å and Fe XII 195 Å data yield a larger number of filaments than the Hα data of the SFC.

Keywords Sun: coronal holes · Sun: filaments · Sun: magnetic field · Automatic detection and classification

1. Introduction

Despite the absence of coronal magnetic-field measurements, the conventional wisdom is that coronal holes are the site of unipolar magnetic-field lines that escape into interplanetary space along with the solar wind. Coronal holes received their name when an almost total absence of emission was first noticed in solar-disk images taken with high-temperature spectral lines in the visible, extreme ultraviolet (EUV), and X rays (*e.g.*, Reeves and Parkinson, 1970; Munro and Withbroe, 1972; Bell and Noci, 1976; Vaiana *et al.*, 1976). Their association with the source of the solar wind was first established when the longitude of a high-speed solar-wind stream measured in interplanetary space in the ecliptic plane was mapped back to the central meridian passage of a coronal hole at the Sun (Krieger, Timothy, and Roelof, 1973; see also Sheeley, Harvey, and Feldman, 1976). If coronal holes are indeed the only source of open magnetic flux at the Sun, then identifying them remains an important task.

Hand-drawn images of coronal holes, spanning almost three decades from 1974 through September 2003, were produced by combining He I images taken with the National Solar Observatory (NSO) Kitt Peak Vacuum Telescope (KPVT), with measurements of the He I equivalent width and photospheric magnetic-field measurements (Harvey, Harvey, and Sheeley, 1982; Harvey and Recely, 2002; Henney and Harvey, 2005). The hand-drawn technique often involved the use of two-day averages of He I 10830 Å spectroheliograms and magnetograms to produce the coronal-hole maps. The unique formation of the He I 10830 Å line in the chromosphere is such that the intensity of this multiplet strongly depends on photoionizing radiation from the overlying upper transition region and corona (Goldberg, 1939). Any reduction of this overlying radiation will lead to a weakening of the He II absorption (Andretta and Jones, 1997; Malanushenko and Jones, 2005), as is believed to occur primarily in coronal holes where the electron density and temperature are lower than the rest of the corona. To date, ground-based observations of the He I 10830 Å line remain the most widely used proxy for estimating the location of coronal holes on the solar disk.

As the size of images and the frequency of observations grow, the automated detection of coronal holes is becoming increasingly important. A number of approaches using the He I ground-based observations have been recently developed (*e.g.*, Henney and Harvey, 2005; Malanushenko and Jones, 2005; de Toma and Arge, 2005). Henney and Harvey (2005) combined He I 10830 Å observations with photospheric magnetograms and developed a scheme to parametrize, *a priori*, the properties of coronal holes as determined originally from the hand-drawn images by Harvey and Recely (2002). The resulting coronal holes were generally in better agreement with EIT Fe XII 195 Å line images than with the hand-drawn coronal-hole maps. Using He I imaging spectroscopy, notably the half-widths and central intensities of the He I 10830 Å line, Malanushenko and Jones (2005) found that the outline of coronal holes on the solar disk agrees with those visually determined from EUV measurements from SOHO/EIT but was not always in agreement with the NSO/Kitt Peak coronal-hole maps. de Toma and Arge (2005) also defined a set of criteria for coronal hole identification, *a priori*, and applied them to synoptic maps. They found that their coronal holes formed a subset of the NSO/Kitt Peak coronal holes.

The advent of coordinated magnetic-field and EUV measurements from the *Solar and Heliospheric Observatory* (SOHO), which cover different phases of the current solar activity cycle, from early 1996 until the present, offers a new opportunity for the automated detection of coronal holes and filaments on the solar disk. Although enticing, the use of EUV lines for the determination of coronal-hole boundaries is not without ambiguity. In fact, the early EUV space observations showed that the intensity of many EUV emission lines is also low near filaments, owing to the low electron densities in the coronal cavity surrounding the filament and the absorption of the surrounding EUV radiation by the cool filament material (*e.g.*, Munro and Withbroe, 1972). Filaments appear as dark, thin, and elongated regions on the solar disk in the Hα 6563 Å line. They are also dark but larger when observed in EUV lines. Hence, any technique developed to determine the location of coronal holes on the solar disk from EUV measurements must contend with the potential ambiguity introduced by the presence of filaments. Consequently, the approach will include criteria to distinguish between the two. Fortunately, coronal holes and filaments have distinct magnetic characteristics. Filaments develop along a polarity-reversal boundary, whereas coronal holes fall within regions with a dominant magnetic polarity.

The goal of this study is to develop an automated approach to detect and classify coronal holes (and by extension also filaments) on the solar disk using EUV data from the Extreme Ultraviolet Telescope (EIT) and photospheric magnetic-field measurements from the Michelson Doppler Imager (MDI) on SOHO. The approach relies on the processing of EUV images to enhance their contrast and on a classification method that relies on their distinct magnetic characteristics.

2. Overview of Approach and Data Selection

The SOHO/EIT data encompass several spectral lines. Consequently, they reflect the behavior of different temperature and density structures in the solar atmosphere. By supplementing the EUV data with the corresponding magnetic-field measurements from SOHO/MDI, it will be shown that the distinct magnetic signatures of coronal holes and filaments contribute significantly to the establishment of a reliable set of criteria. The detection of these candidate features thus defined will be compared with existing feature catalogs. These consist of *i*) the catalog of coronal-hole maps from NSO/Kitt Peak synoptic maps generated from He I 10830 Å observations and *ii*) the Solar Feature Catalog (SFC), an on-line database built in the framework of the European Grid of Solar Observations (EGSO) project (Bentley, Csillaghy, and Scholl, 2004) and implemented at Bradford University (Zharkova *et al.*, 2005). It contains detailed descriptions of filaments, sunspots, and active regions, detected automatically from the Observatoire de Paris/Meudon and MDI observations.

The following SOHO keywords have been used to select the EUV data and magnetograms needed. The EUV/EIT data (Delaboudinière *et al.*, 1995) selected from the SOHO archive correspond to *i*) level zero data, with *ii*) science objective as "FULL SUN 171/284/195/304," and *iii*) object as "full FOV." The data thus consist of four synoptic full-disk and full-resolution images taken, in general, every six hours at the four wavelengths, one at the chromosphere/transition region interface (He II 304 Å) and three corresponding to coronal temperatures (Fe IX/X 171, Fe XII 195, and Fe XV 284 Å). Because the Fe XV 284 Å data lack the necessary contrast for detection purposes, they will not be considered in this study.

The magnetograms from SOHO/MDI (Scherrer *et al.*, 1995) are used to compute the magnetic-field intensity and polarity. Criteria to select these data from the archive are

i) level 1.8, with the most recent calibrated algorithm applied, and *ii*) the observing mode as "FD_Magnetogram_Sum." The data thus retrieved correspond to synoptic magnetograms taken every 96 minutes with an average of five magnetograms. The noise level for this type of data is 9.2 G (Liu, Zhao, and Hoeksema, 2004). Prior to any analysis, the quality of the selected data, such as absence of telemetry gaps and instrumental problems, is checked.

Since comparisons will be made among the features determined from the combined EIT/MDI data, the NSO/Kitt Peak coronal-hole maps, and the SFC, it is important to consider the time in selecting the data to be analyzed. The observing times must be as close as possible to one another. They are therefore selected in the following order: *i*) Kitt Peak, *ii*) SFC, *iii*) EIT, and *iv*) MDI, to minimize the assumptions made regarding the evolution of different features and the corresponding magnetic field.

3. Data Preparation and Image Processing

Given that the data originate from different sources, that they are not identically co-temporal, and that the images are not the same size (*i.e.*, the pixel resolution is not the same in the EIT and MDI images), the following steps must first be taken: *i*) a given time of observation is identified, and all observations are scaled to match in size and time (*i.e.*, rotation). *ii*) Image-processing techniques are then applied to the data thus matched to extract candidate features. In what follows, the details of these two steps are presented.

To be able to compute magnetic-field intensity and polarity on extracted features, EIT images and MDI magnetograms must be first co-aligned in spatial resolution (*i.e.*, pixel size, center of the disk, and radius) and rotation. To keep the magnetic-field values intact, the EIT data are aligned with respect to the MDI data.[1] Therefore, using the strict data selection process given in Section 2 minimizes the rotation to be applied to each observation. It is found that when overlapping SFC contours, their coordinates have to be rotated to match the observing time of the magnetogram. Finally, NSO/Kitt Peak maps are also co-rotated when needed.

A suite of image-processing operations (Gonzalez and Woods, 2002) has been implemented for the different wavelengths in the EUV EIT images. Once the images are calibrated using the standard EIT routines, the following steps, which are summarized in Table 1, are implemented: *i*) normalize the images (*i.e.*, eliminate effects from the variability of the Sun, such as nonuniform illumination and center-to-limb variation, as well as detector-aging effects), *ii*) apply filters for noise cleaning (*i.e.*, apply smoothing and spatial linear filters and very bright pixel removal), *iii*) enhance the contrast through histogram equalization (Gonzalez and Woods, 2002; Pizer *et al.*, 1987), and *iv*) apply an image-segmentation technique based on a combination of region-based and edge-based methods. The regions of interest are subsequently extracted, and a final cleanup is performed, which consists of removing small features. The candidate features are identified so that the next step involving comparison with the magnetograms, and thus final classification, can be initiated.

These steps are not performed in exactly the same manner for all wavelengths. Although Fe IX/X 171 Å and Fe XII 195 Å images are treated in an identical manner, the He II 304 Å images are not. For the latter, the global contrast needs to be enhanced to enable the image segmentation and contour extraction because of the higher level of spatial detail

---

[1]See the "IDL Map Software for Analyzing Solar Images" package for SolarSoft (http://orpheus.nascom. nasa.gov/~zarro/idl/maps/maps.html).

Table 1 Summary of image-processing operations.

Step	Operations	Detailed operations per wavelength		
		304 Å	171 Å	195 Å
1	Calibration	Standard EIT routine		
2	Normalization	Smoothing spatial linear filter		
		(filter out pixels brighter than their surrounding area)		
		Log scaling	n/a	
3	Limb darkening removal	Low-pass filter	n/a	
4	Contrast enhancement	Histogram equalization (range parameters depend on the solar cycle period)	Local histogram equalization	
5	Image segmentation: histogram-based and region-growing methods	– Smoothing to connect closed dark small features	– Smoothing to connect closed dark small features	
		– Thresholding (binary transformation)	– Histogram equalization to isolate darkest features	
			– Thresholding (binary transformation)	
			– morphological erode operation	
		– Limb and disk center are processed with different parameters	– Steps 4 and 5 are executed three times for 171 Å and twice for 195 Å to extract feature of different sizes	
		– Results are combined together	– Results are combined together	
6	Regions of interest extraction	Based on contour method		
7	Final cleanup	Remove small features		
		<300 pixels	<1000 pixels	
8	Region label	Identification of all features for next step		
		(magnetic-profile computation and classification)		

observed at this wavelength. For the 171 and 195 Å images, the local-contrast enhancement is needed to reveal candidate features that could be hidden either because of excessive brightness, such as for features close to an active region, or because of poor contrast. In the former case, the features in the neighborhood of an active region can only be revealed when images are processed locally. In the latter case, for large dark regions generally believed by default to be coronal holes, slight changes in brightness are flattened and become invisible without a local enhancement. In both cases, the local-contrast enhancement is such that the dynamic range in brightness is reduced, and the contrast is increased (Stark, 2000). The main side effect of this technique is the enhancement of noise or small spatial details, but no artificial features are created (Gonzalez and Woods, 2002).

## 4. Candidate Features: Detection and Classification Method

The image-processing detection technique described in the previous section enables the extraction of candidate features, namely coronal holes and filament channels. Without process-
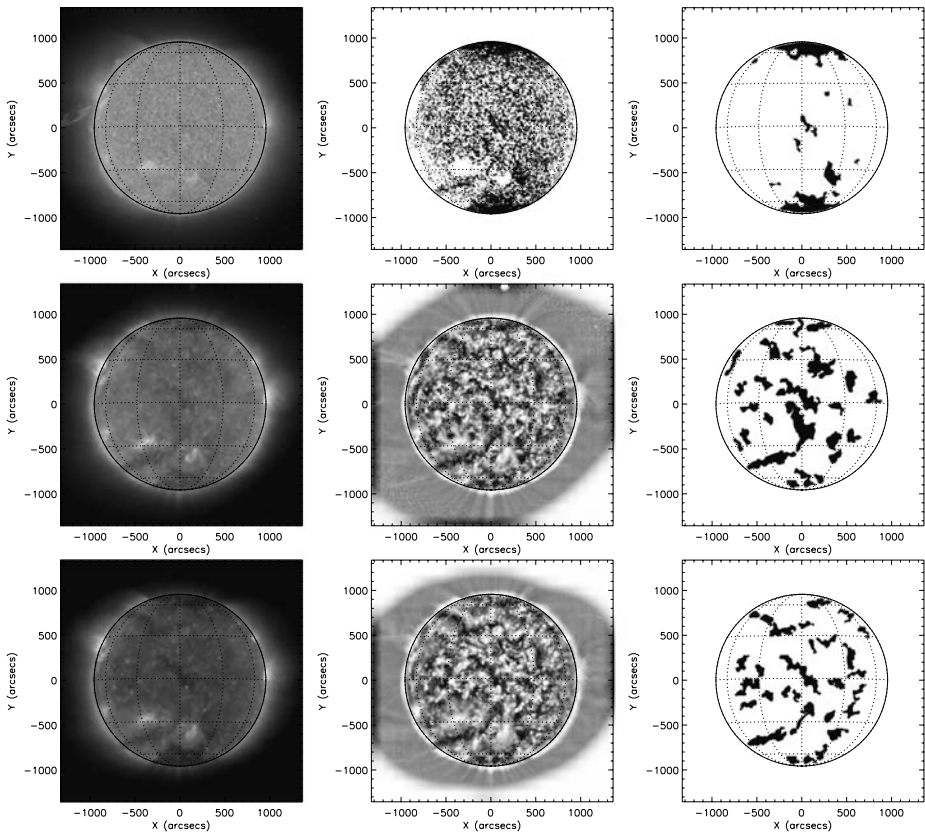
Figure 1 Example of SOHO/EIT data from solar minimum, on 27 May 1997. The top row corresponds to He II 304 Å, the middle row to Fe IX/X 171 Å, and the bottom row to Fe XII 195 Å data from SOHO/EIT. The left panels show the original data, the middle panels show the processed images, and the right panels show the detected candidate features (*i.e.*, coronal holes and filaments).

ing, the images do not have enough contrast to provide means for an automated detection process (see Scholl, 2003). Three examples were selected from dates coinciding with solar minimum (Figure 1), solar maximum (Figure 2), and the declining phase of the solar cycle (Figure 3). In each of these figures there are three rows consisting of three panels each. The top row corresponds to the He II 304 Å data, the middle to Fe IX/X 171 Å, and the bottom to Fe XII 195 Å. The left panel in each row shows the original EIT image, the middle one gives the EIT image after processing, and the right panel shows the candidate features extracted from the image processing, that is, filaments and coronal holes without distinction, placed on a Stonyhurst disk. Upon comparison of the left (original images) and middle panels (processed images) in each row, it is clear that the processing brings out far more detail.

At this point there is no other way to distinguish between coronal holes and filaments, as their characteristics in all of the EIT EUV images, both unprocessed and processed, are the same since they all appear as dark regions. There is also a significant variation in the number, size, and shape of these features depending on the spectral line considered, as seen in the examples of Figures 1–3.
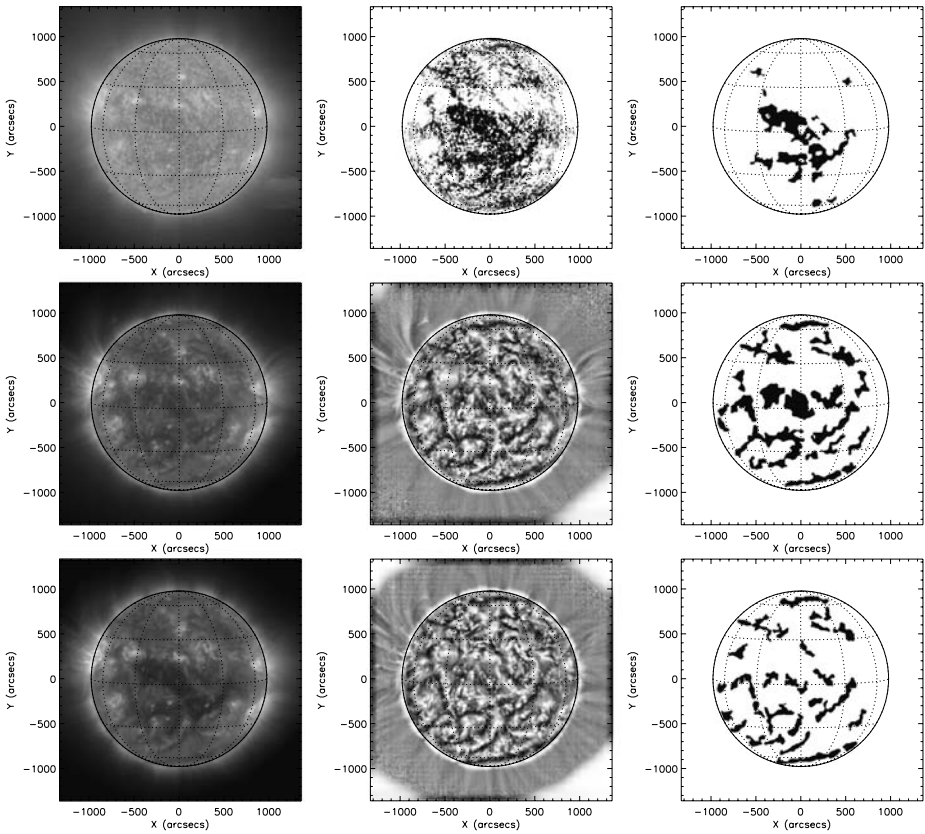
Figure 2 Same as Figure 1 for solar maximum on 6 November 1999.

Once all candidate features have been isolated from each observation, the surface of the feature is mapped onto the corresponding magnetogram to extract the corresponding magnetic-field intensity and net polarity. From this step, two categories of objects emerge: one is characterized by a dominant polarity, supported by a significant percentage of strong values, mostly of one polarity; the other category has an average intensity close to zero, with no strong values. The skewness of the distribution is also very different between the two.

To improve on these findings, a set of statistical estimators has been used. To establish the magnetic polarity within a given feature, the weighted mean (net flux), the sum of the field strengths in both polarities, the average of the two maximal values in each polarity, the skewness (and its sign) of the real magnetic-field distribution, and the relative magnetic-flux imbalance ($\langle B_z \rangle / \langle |B_z| \rangle$) are used. Furthermore, to analyze the distribution of the magnetic-field intensity underlying a given feature, a simplified histogram with bins of < -170, $-120, -70, -20, 20, 70, 120$ and > 170 G is computed. This simplified distribution reveals the nature of most filament channels. The noise level within the magnetograms is taken into account in two different ways: each estimator is computed with and without the noise and both results must agree if the percentage of values within the noise is not too excessive (*i.e.*, $< 70\%$).

Typical magnetic-field profiles for features selected from Figures 1–3 are shown in Figures 4–6. The top row in each figure corresponds to a filament channel, and the bottom one
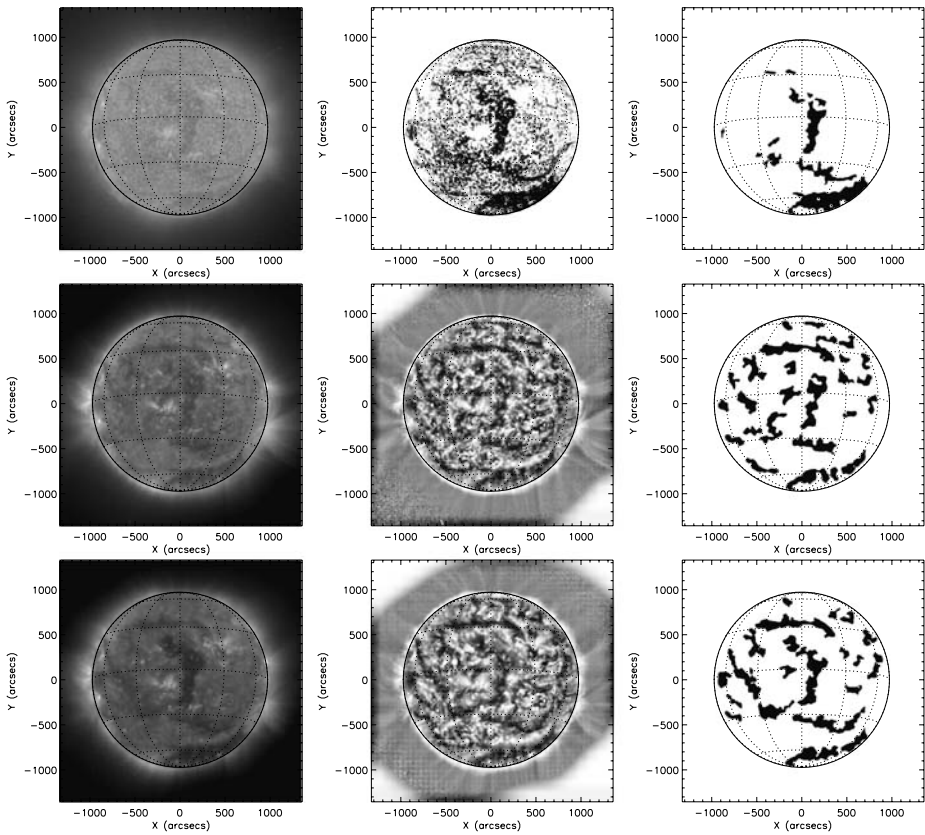
Figure 3 Same as Figure 1 for the declining phase of the solar cycle on 23 March 2003.

to a coronal hole. The left panel in each row shows the candidate feature. The middle panel is a histogram of the line-of-sight magnetic-field intensity, B_z, within the given area of the feature. The right panel is the same histogram but with the magnetic-field values binned.

Among all these estimators (see the summary in Table 2), the most significant and discriminating one is the relative magnetic-flux imbalance. Other discriminators, which are not used during the classification itself (but only during the manual analysis of the features), allow us to specify two typical magnetic profiles: a coronal hole is always associated with a relative magnetic-flux imbalance > 0.15, a skewness of the intensity distribution ≈ 0.7, and a mean > 1. All estimators have the same sign, including the sum of the field strength (*i.e.*, the number of pixels of the dominant polarity is always greater than the number of pixels of the other polarity), and the minimum field intensity is > 70 G. For most filament channels, the relative magnetic-flux imbalance is < 0.15, the skewness of the intensity distribution is $\approx < 0.7$, and the mean is around 0. Not all estimators have the same sign, and the maximum intensity is < 70 G (with very few values above 70 G).

Although these estimators lead to a clear separation between coronal holes and filament channels, a few outstanding issues remain in this classification scheme: *i*) features located close to the limb can lead to a wrong classification owing to the poor resolution in these areas. *ii*) Features too close to an active region can have strong magnetic-field values, probably coming from the active region itself. Such is the case, for example, of two features in
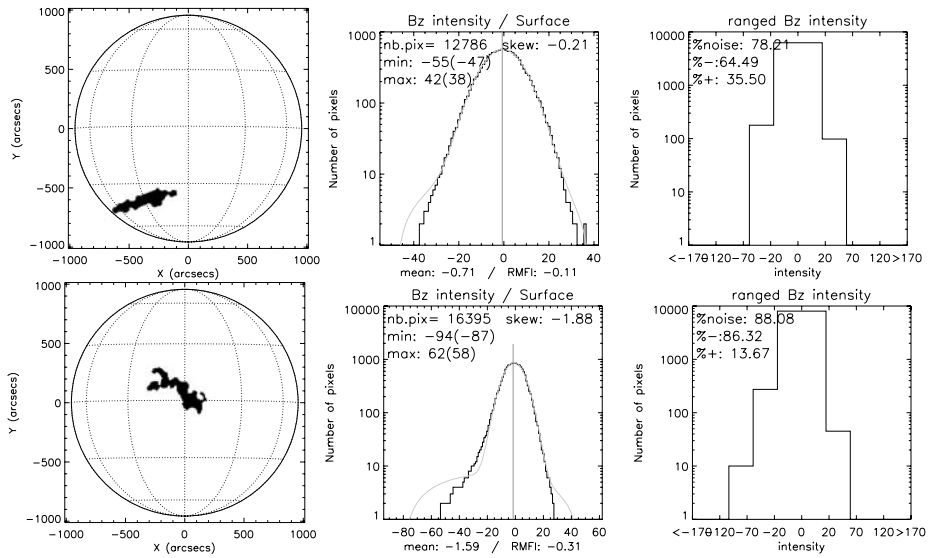
Figure 4 Left panels: Sample candidate filament (top) and coronal hole (bottom) for solar minimum, on 27 May 1997. Middle panels: Histogram of the line-of-sight magnetic-field intensity within the corresponding feature. Also shown in these panels is the skewness, the size in pixels, the relative magnetic-flux imbalance (RMFI), the maximum and minimum intensities for each polarity, and the mean. Right panels: Corresponding histogram of the line-of-sight magnetic-field intensity for magnetic-field values binned as < -170, -120, -70, -20, 20, 70, 120, and > 170 G. The percentage of pixels for each polarity is also shown as well as the percentage of pixels within the noise level.

Table 2 Summary of magnetic profiles for candidate features.

Magnetic profiles	Coronal holes	Filament channels
Relative magnetic-flux imbalance (RMFI)	> 0.15 G	< 0.15 G
Skewness	> 0.17	< 0.17
Weighted mean	> 1	≈ 0
Intensity range	$\approx 70 - 170$ G	$\approx < 70$ G
Estimators sign	All > 0 or all < 0	Mix of both signs

Figure 8, at coordinates $(-250, -300)$ and $(600, -400)$, where in He II and Fe XII the features are identified as filaments, but as a coronal hole in Fe IX/X. This is likely due to the lack of precision in the contour detection process itself, especially for Fe IX/X 171 and Fe XII 195 Å lines corresponding to hot plasmas, but not for the cooler plasma emitting at He II 304 Å. *iii*) Some filament channels exhibit the same profile as coronal holes. *iv*) For a coronal hole close to the limb the histogram may have the same shape as that of a filament channel. *v*) The percentage of high values in all cases may not be significant for very small features with sizes less than 2000 pixels, even though the mean can still be strong.
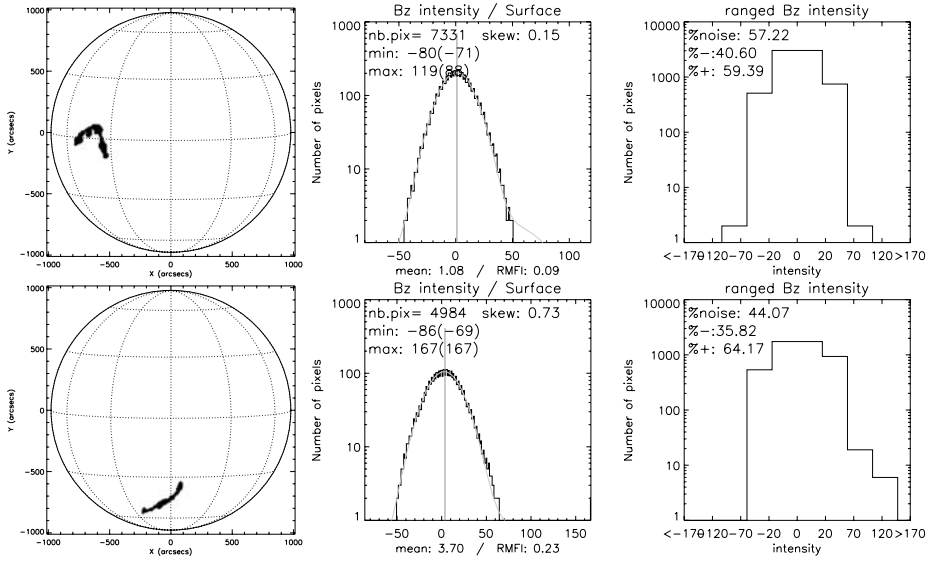
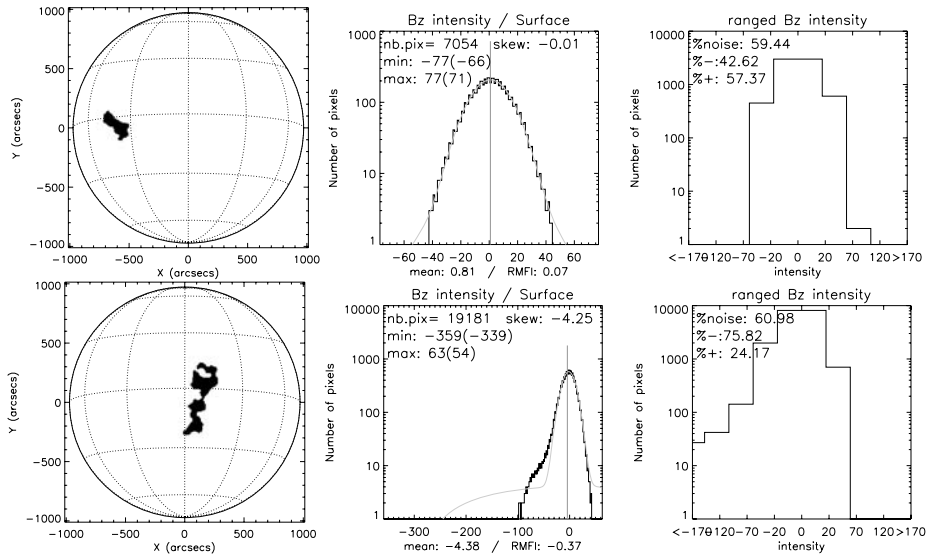**Figure 5** Same as Figure 4 for solar maximum on 6 November 1999.

**Figure 6** Same as Figure 4 for the declining phase of the solar cycle on 23 March 2003.

5. Candidate Features: Final Product

Figures 7 – 9 show the results of the application of these described criteria to the classifica-
tion of the features shown in Figures 1 – 3 for the three wavelengths He II 304 Å (top row),
Fe IX/X 171 Å (middle rows), and Fe XII 195 Å (bottom rows). Figure 7 is an example from
solar minimum, Figure 8 from solar maximum, and Figure 9 from the declining phase of
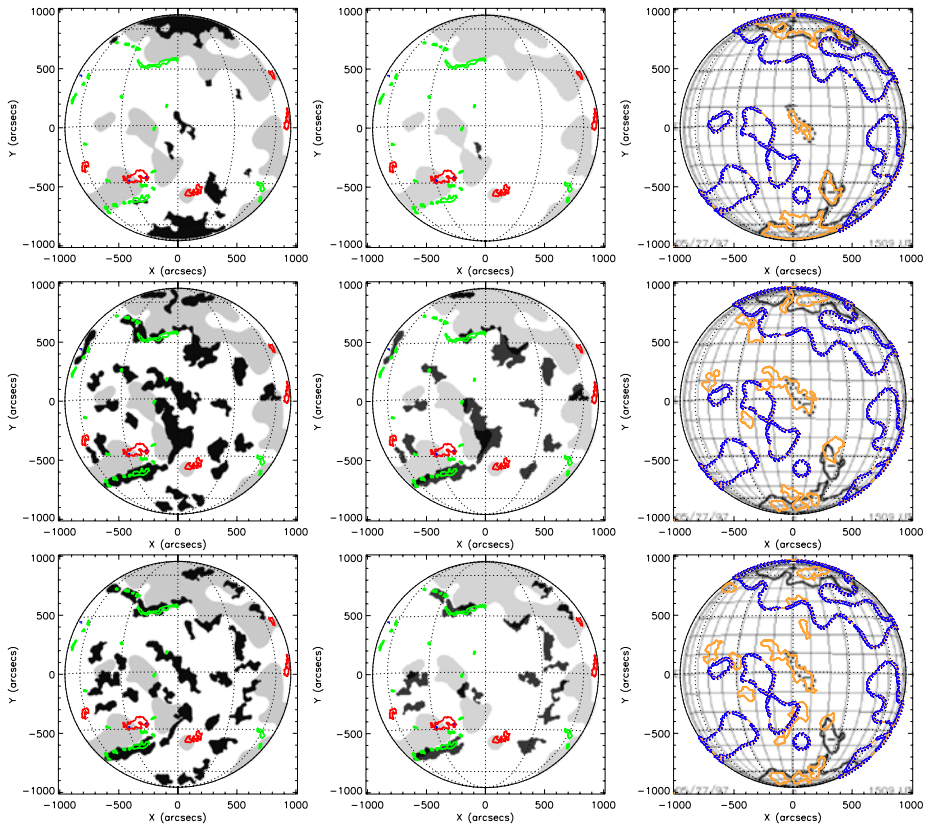
Figure 7 Example of feature classification at solar minimum, on 27 May 1997. The top row corresponds to He II 304 Å, the middle row to Fe IX/X 171 Å, and the bottom row to Fe XII 195 Å data from SOHO/EIT. In the left panels, all candidate features, both coronal holes and filaments, detected with the method presented here, are shown in black. Shown in red are active regions, the blue dots indicate sunspots, and the green contours are filaments, all taken from the SFC. The background, in this and the middle panel, is the result of the time-corresponding processed magnetogram from SOHO/MDI, as described in Scholl (2003), where the white areas represent the dominant negative polarity, and the gray the dominant positive polarity. In the middle panels, the filament channels detected are shown in black together with the same filaments (green) and active regions (red) from the SFC also shown in the left panels. In the right panels, the detected coronal holes are shown as orange contours plotted on a Stonyhurst grid together with the NSO/Kitt Peak coronal holes given as black contours. The double solid-dashed blue line is the demarcation line between the opposite-polarity magnetic-field areas shown as gray and white in the two left panels.

the solar cycle. In the left panels of each row, the candidate features are shown in black. (Note that these are the same features shown in the right panels of Figures 1–3, which were derived from the image processing step.) The red contours correspond to active regions, the blue dots to sunspots, and the green contours to filament channels, all taken from the SFC. The white and gray backgrounds in the left and middle panels represent the dominant negative and positive polarities, respectively, in the MDI processed magnetogram. As described by Scholl (2003), the magnetogram is treated as an image. It is smoothed to eliminate small scales. A line is subsequently drawn that separates pixels with opposite signs (*i.e.*, polarities).
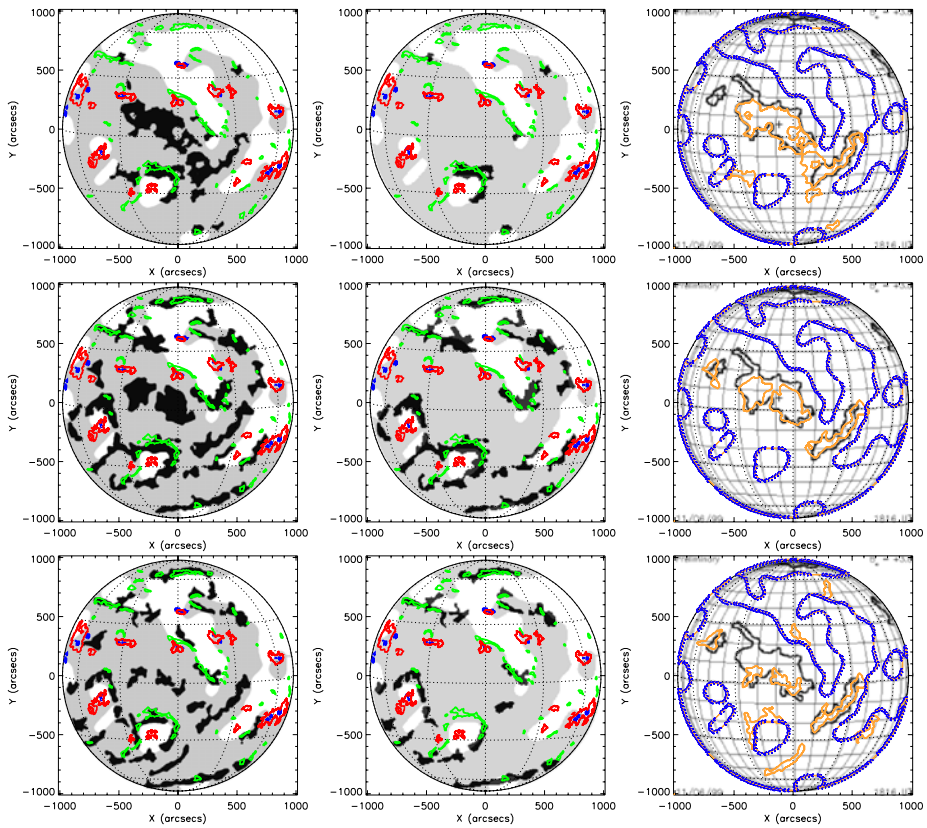
Figure 8 Same as Figure 7 for solar maximum on 6 November 1999.

In these figures, the filament channels and coronal holes have been separated in the middle and right panels. The middle panels show the filament channels as identified from the application of the magnetic-field criteria, plotted together with the active regions (red) and filament channels (green) given by the SFC. The yellow contours in the right panels are the detected coronal holes plotted on a Stonyhurst disk together with the black contours of the NSO/Kitt Peak coronal holes. In the right panels the polarity inversion line from the processed magnetogram is given as a thick blue line.

Several expected results emerge from these figures, together with some unexpected ones. In general, there are more candidate features, both filaments and coronal holes, detected with this approach than those appearing in the SFC or NSO/Kitt Peak coronal-hole maps. Furthermore, the numbers, sizes, and distribution of candidate features are not the same at all wavelengths.

Consider first the filaments, which are shown separately in the middle panels of Figures 7 – 9. At solar minimum (Figure 7), only one small filament is detected in He II 304 Å, which does not correspond spatially with any of the SFC filaments. However, the Fe IX/X 171 and Fe XII 195 Å images yield more filaments than present in the SFC, albeit not necessarily all the same at these two wavelengths. At solar maximum (Figure 8), there are more filaments detected in He II 304 Å than at solar minimum, with some corresponding very well with those in the SFC. Overall, the correspondence between filaments detected in 171 and
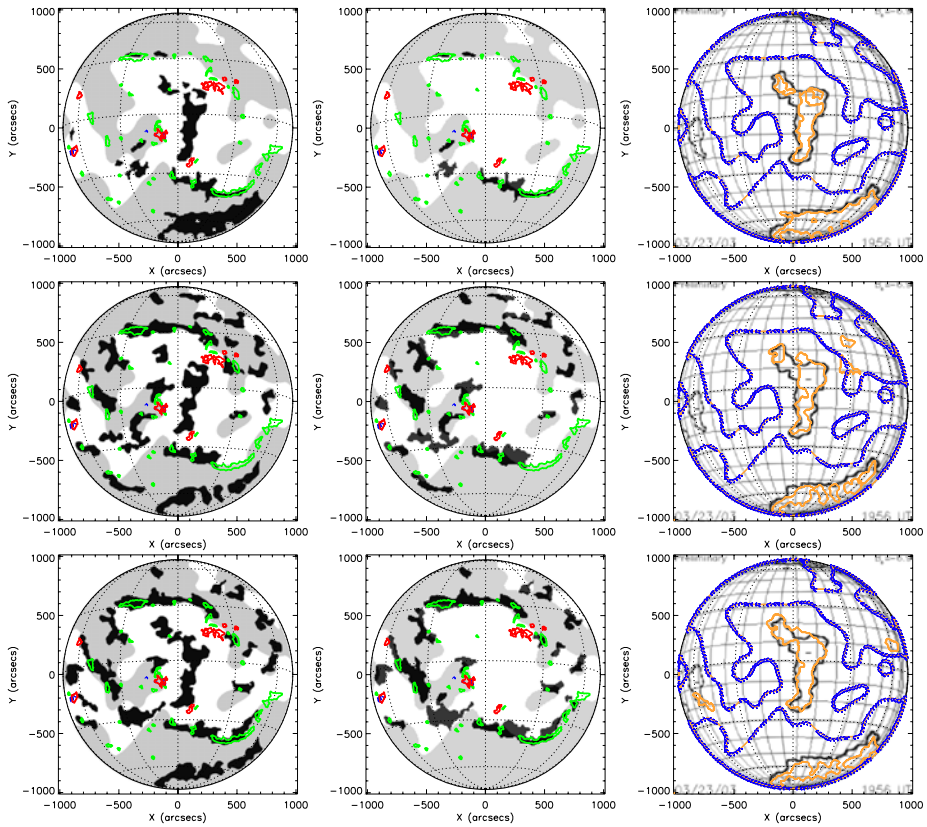
Figure 9 Same as Figure 7 for the declining phase of the solar cycle on 23 March 2003.

195 Å and the SFC is much better than the solar minimum case, with a few minor exceptions. This is also the case during the declining phase of the solar cycle (Figure 9). Comparison with the underlying magnetograms shows that the shape of filaments follows the magnetic reversal line very nicely in many places. This is particularly striking at solar maximum and the declining phase of solar activity. There are a few exceptions at solar minimum.

For coronal holes, there seems to be a much better correspondence with the NSO/Kitt Peak coronal holes, than the correspondence between candidate filaments and the SFC filaments, as previously noted. In some cases, there are more coronal holes than NSO/Kitt Peak ones. All detected holes lie in magnetic regions with a dominant polarity, as seen from comparison with the magnetograms in the left panels. It is not surprising that the He II 304 Å coronal hole contours are the closest to those defined in the He I 10830 Å NSO/Kitt Peak coronal-hole maps, as originally reported by Harvey and Sheeley (1977). It also seems that the Fe XII 195 Å maps yield finer, narrower, and more numerous coronal holes than the other wavelengths. The best correspondence between the coronal holes detected in all wavelengths and the NSO/Kitt Peak coronal-hole maps is found during the declining phase of the solar cycle (see right panels of Figure 9).

Finally, we note that the location of active regions is given in Figures 7–9 because of their impact on the statistical estimators of the magnetic field when a coronal hole or a filament is in their vicinity.

6. Discussion and Conclusion

The automated approach described here, for the detection of, and the distinction between, coronal holes and filaments in EUV images of the solar disk, is based on the processing of the SOHO/EIT coronal images and the identification of distinct magnetic signatures from the corresponding magnetograms. Although sharing the same apparent visual signatures in all the EUV wavelengths considered, this study shows that coronal holes and filaments are characterized by well-defined and distinct magnetic signatures.

Comparison with other databases for coronal holes and filaments, namely the NSO/Kitt Peak catalog of coronal-hole maps and the Solar Feature Catalog for filaments, shows a good correspondence between the candidate features detected in this study and those present in these catalogs. There are however notable discrepancies. In general, more features are detected in this approach than are present in the catalogs, with the exception of examples from solar minimum. This could likely be due to the low contrast in the EIT images during that time period. It is not evident, *a priori*, whether this problem will be resolved in the future with better-quality data, as expected from the STEREO mission. As originally noted by Harvey and Sheeley (1977), the comparison between He I 10830 Å and He II 304 Å images does not always yield consistent results, and the same holds true for the other EUV wavelengths considered here. For features lying close to Sun center, when line-of-sight effects are minimal, a one-to-one correspondence between the different data sets is found for both coronal holes and filaments.

Interestingly, this automated technique reveals features close to active regions that would not have been detected otherwise. In those cases, the detection can sometimes be ambiguous as filaments are often found to have large magnetic-field intensity values, making them indistinguishable from coronal holes.

As is amply evident from the examples presented here, the richness of the EUV data can be a drawback. It is not clear whether a unique set of criteria can be defined to design a robust automated detection scheme. Why the process leads to differences among the three wavelengths is not evident. Nonetheless, there is no metric, or physical reason, to assume that the He I 10830 Å line, which has been used as a diagnostic tool for coronal holes for over three decades, is indeed the most reliable metric. There is no doubt that the variety of temperatures, densities, and sizes of magnetic structures extending in the corona, which lead to differences in the EUV images, impact the detection process, in particular the distinction between open and closed magnetic structure – an ambiguity that is further aggravated by line-of-sight effects.

There are several considerations that might lead to a better and more consistent automation in future studies. One can take advantage of a time sequence for ambiguous cases to see if a feature (*i.e.*, either a coronal hole or filament channel) maintains its magnetic characteristics as it traverses the solar disk, and as the effect of the line of sight varies. This next step will lead to the construction of a coronal-hole catalog that will use the time tracking method described in Aboudarham *et al.* (2007).

In summary, this scheme differs from other automated coronal-hole detection techniques (*e.g.*, Henney and Harvey, 2005; de Toma and Arge, 2005) as no criteria for their detection are identified *a priori* here. Although robust, the proposed automated approach is by no means complete, and it should be considered complementary to other published approaches. One of its strengths is that it is the first to consider the role of filament channels. With the advent of the STEREO mission, it should become possible to define additional criteria for the automated detection of coronal holes and filaments, as these features might become visually distinguishable in higher spatial resolution images.

References

Aboudarham, J., Scholl, I., Fuller, N., Fouesneau, M., Galametz, M., Gonon, F., Maire, A., Leroy, Y.: 2007, Automatic detection and tracking of filaments to fill-in a solar feature database. *Ann. Geophys.*, in press.

Andretta, V., Jones, H.P.: 1997, On the role of the solar corona and transition region in the excitation of the spectrum of neutral helium. *Astrophys. J.* **489**, 375 – 394.

Bell, B., Noci, G.: 1976, Intensity of the Fe XV emission line corona, the level of geomagnetic activity, and the velocity of the solar wind. *J. Geophys. Res.* **81**, 4508 – 4516.

Bentley, R.D., Csillaghy, A., Scholl, I.: 2004, The European grid of solar observations. In: Quinn, P.J., Bridger, A. (eds.) *Optimizing Scientific Return for Astronomy through Information Technologies, Proc. SPIE* **5493**, 170 – 177.

Delaboudinière, J.P., Artzner, G.E., Brunaud, J., Gabriel, A.H., Hochedez, J.F., Millier, F., Song, X.Y., Au, B., Dere, K.P., Howard, R.A., Kreplin, R., Michels, D.J., Moses, J.D., Defise, J.M., Jamar, C., Rochus, P., Chauvineau, J.P., Marioge, J.P., Catura, R.C., Lemen, J.R., Shing, L., Stern, R.A., Gurman, J.B., Neupert, W.M., Maucherat, A., Clette, F., Cugnon, P., van Dessel, E.L.: 1995, EIT: extreme-ultraviolet imaging telescope for the SOHO mission. *Solar Phys.* **162**, 291 – 312.

de Toma, G.D., Arge, C.N.: 2005, Multi-wavelength observations of coronal holes. In: Sankarasubramanian, K., Penn, M., Pevtsov, A. (eds.) *Large-scale Structures and Their Role in Solar Activity*, *CS-**346**, Publ. Astron. Soc. Pac., San Francisco, 251 – 260.

Goldberg, L.: 1939, Transition probabilities for He I. *Astrophys. J.* **90**, 414 – 428.

Gonzalez, R.C., Woods, R.E.: 2002, *Digital Image Processing*, Addison-Wesley Longman, Boston.

Harvey, J.W., Sheeley, N.R. Jr.: 1977, A comparison of He II 304 Å and He I 10830 Å spectroheliograms. *Solar Phys.* **54**, 343 – 351.

Harvey, K.L., Recely, F.: 2002, Polar coronal holes during cycles 22 and 23. *Solar Phys.* **211**, 31 – 52.

Harvey, K.L., Harvey, J.W., Sheeley, N.R. Jr.: 1982, Magnetic measurements of coronal holes during 1975–1980. *Solar Phys.* **79**, 149 – 160.

Henney, C.J., Harvey, J.W.: 2005, Automated coronal hole detection using He 1083 nm spectroheliograms and photospheric magnetograms. In: Sankarasubramanian, K., Penn, M., Pevtsov, A. (eds.) *Large-scale Structures and Their Role in Solar Activity*, *CS-**346**, Publ. Astron. Soc. Pac., San Francisco, 261 – 268.

Krieger, A.S., Timothy, A.F., Roelof, E.C.: 1973, A coronal hole and its identification as the source of a high velocity solar wind stream. *Solar Phys.* **29**, 505 – 525.

Liu, Y., Zhao, X., Hoeksema, T.: 2004, Correction of offset in MDI/SOHO magnetograms. *Solar Phys.* **219**, 39 – 53.

Malanushenko, O.V., Jones, H.P.: 2005, Differentiating coronal holes from the quiet Sun by He 1083 nm imaging spectroscopy. *Solar Phys.* **226**, 3 – 16.

Munro, R.H., Withbroe, G.L.: 1972, Properties of a coronal "hole" derived from extreme-ultraviolet observations. *Astrophys. J.* **176**, 511 – 520.

Pizer, S.M., Amburn, E.P., Austin, J.D., Cromartie, R., Geselowitz, A., Greer, T., Romeny, B.T.H., Zimmerman, J.B.: 1987, Adaptive histogram equalization and its variation. *Comput. Vision Graphics Image Process.* **39**(3), 355 – 368.

Reeves, E.M., Parkinson, W.H.: 1970, An atlas of extreme-ultraviolet spectroheliograms from OSO-IV. *Astrophys. J. Suppl. Ser.* **21**, 405 – 409.

Scherrer, P.H., Bogart, R.S., Bush, R.I., Hoeksema, J.T., Kosovichev, A.G., Schou, J., Rosenberg, W., Springer, L., Tarbell, T.D., Title, A., Wolfson, C.J., Zayer, I., MDI Engineering Team: 1995, The solar oscillations investigation – Michelson Doppler imager. *Solar Phys.* **162**, 129 – 188.

Scholl, I.: 2003, Conception, réalisation et utilisation d'archives de données solaires spatiales. Ph.D. thesis, Université Paris 6, France.

Sheeley, N.R. Jr., Harvey, J.W., Feldman, W.C.: 1976, Coronal holes, solar wind streams, and recurrent geomagnetic disturbances – 1973 – 1976. *Solar Phys.* **49**, 271 – 278.

Stark, J.A.: 2000, Adaptive image contrast enhancement using generalizations of histogram equalization. *IEEE Trans. Image Process.* **9**(5), 889 – 896.

Vaiana, G.S., Zombeck, M., Krieger, A.S., Timothy, A.F.: 1976, ATM observations – X-ray results. *Astrophys. Space Sci.* **39**, 75 – 101.

Zharkova, V.V., Aboudarham, J., Zharkov, S., Ipson, S.S., Benkhalil, A.K., Fuller, N.: 2005, Solar feature catalogues in EGSO. *Solar Phys.* **228**, 361 – 375.